

Use of Rayleigh imaging and ray tracing to correct for beam-steering effects in turbulent flames

Sebastian A. Kaiser, Jonathan H. Frank, and Marshall B. Long

Laser Rayleigh imaging has been applied in a number of flow and flame studies to measure concentration or temperature distributions. Rayleigh cross sections are dependent on the index of refraction of the scattering medium. The same index of refraction changes that provide contrast in Rayleigh images can also deflect the illuminating laser sheet. By applying a ray-tracing algorithm to the detected image, it is possible to correct for some of these beam-steering effects and thereby improve the accuracy of the measured field. Additionally, the quantification of the degree of beam steering through the flow provides information on the degradation of spatial resolution in the measurement. Application of the technique in a well-studied laboratory flame is presented, along with analysis of the effects of image noise and spatial resolution on the effectiveness of the algorithm. © 2005 Optical Society of America

OCIS codes: 120.1740, 100.2000, 290.5870.

1. Introduction

Planar laser imaging has become one of the most widely used laser diagnostic techniques applied to the study of combustion and gas dynamic flow fields. The ability to record the spatial distribution of quantities of interest provides true insight into these complex systems. The work of R. K. Hanson's group over more than 25 years has been instrumental in pushing the boundaries of laser imaging techniques.¹⁻³ Planar laser-induced fluorescence (PLIF) techniques are particularly useful for their ability to measure trace species, temperature, pressure, and even velocities in a wide variety of environments.

Laser Rayleigh scattering is among the most easily implemented laser imaging techniques for measurements in reacting and nonreacting flows. Since Rayleigh scattering is an elastic process, it does not require a specific laser wavelength for its implementation but simply requires enough laser energy for a sufficient signal. A broad range of commercially avail-

able laser sources is suitable for Rayleigh measurements. Depending on the particular flow being studied, Rayleigh scattering has been used to study nonreactive mixing,^{4,5} as well as temperature⁶⁻⁹ and fuel concentration¹⁰ in flames. Because the signals are relatively strong and their interpretation straightforward, Rayleigh scattering has been used extensively for quantitative imaging measurements.

The Rayleigh signal from a volume of gas depends on the scattered intensity at the detector and can be expressed as follows:

$$S_{\text{Ray}} = KI_0 NV \sum_i x_i \sigma_i = KI_0 NV \sigma_{\text{eff}}, \quad (1)$$

where K is a constant dependent on the experimental configuration, I_0 is the intensity of incident laser light, and N is the number density of molecules in the probe volume, V . The summation is over all species, with x_i the mole fraction and σ_i the Rayleigh cross section of the i th gas in the mixture. The summation term is often collected into a single, effective Rayleigh scattering cross section, σ_{eff} .

The Rayleigh cross section is related to the local index of refraction, n , by the expression¹¹

$$\sigma = \frac{24\pi^3}{\lambda^4 N^2} \left(\frac{n^2 - 1}{n^2 + 2} \right)^2, \quad (2)$$

with λ the wavelength of light and, as before, N the

S. A. Kaiser and M. B. Long (marshall.long@yale.edu) are with the Department of Mechanical Engineering, Yale University, P.O. Box 208284, New Haven, Connecticut 06520. J. H. Frank is with the Combustion Research Facility, Sandia National Laboratories, P.O. Box 969, Livermore, California 94551.

Received 2 February 2005; revised manuscript received 19 May 2005; accepted 20 May 2005.

0003-6935/05/316557-08\$15.00/0

© 2005 Optical Society of America

number density of scatterers (neglecting depolarization effects). It should be noted that both N and n are for the local conditions of temperature and pressure and that σ represents the total (rather than differential) cross section. For gases the index of refraction is very close to one, and the approximation

$$\frac{(n^2 - 1)}{(n^2 + 2)} \approx \frac{2}{3} (n - 1) \quad (3)$$

is often made. Combining relations (1)–(3) gives an expression for the Rayleigh signal in terms of the index of refraction:

$$S_{\text{Ray}} = KI_0 V \frac{32\pi^3}{3\lambda^4} \frac{(n - 1)^2}{N}. \quad (4)$$

This formulation makes it clear that the Rayleigh signal carries information on the local index of refraction of the gas mixture. The same variations in the local index of refraction that generate contrast in the Rayleigh image of a flow or flame can also cause beam steering of the illuminating laser sheet. The beam steering of the laser sheet is a specific case of the more general problem of the distortion of wavefronts propagating in turbulent media. There has been considerable work done on this topic by the aero-optics community. Dimotakis *et al.*¹² provide useful references to this work and demonstrate the use of a Fourier transform filter approach to correct for beam-steering effects. If the Rayleigh image can be used to infer the local index of refraction, then it may be possible to use this information to characterize the beam steering caused by the flow and perhaps even correct for its effects.

For a given experiment with a fixed laser intensity and wavelength, the index of refraction will depend on the Rayleigh signal and local number density according to

$$n - 1 \propto \sqrt{S_{\text{Ray}} N}. \quad (5)$$

As mentioned previously, Rayleigh scattering can be used to study flows in several different circumstances. In an isothermal flow, Rayleigh scattering can be used to measure the mixing of two gases with different Rayleigh cross sections.^{4,5} In this case, the number density, N , will be constant and the local index of refraction will simply be proportional to the square root of the Rayleigh signal:

$$n - 1 \propto \sqrt{S_{\text{Ray}}} \quad (6)$$

Rayleigh scattering can also be used to monitor temperature variations (i.e., variations in N) in a gas or gas mixture in which the Rayleigh cross section is constant. Examples of this type of application would be that of a heated jet mixing with ambient-temperature gas of the same composition, or a flame

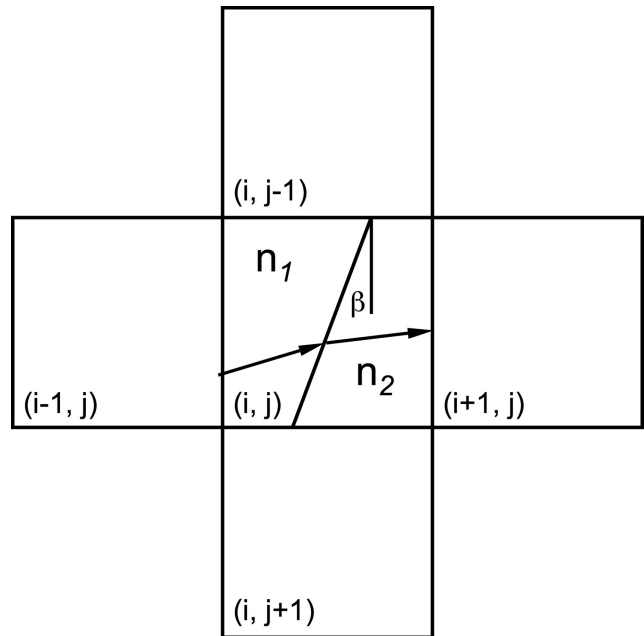


Fig. 1. Pixel stencil used in the ray-tracing implementation.

in which the fuel, oxidizer, and products are specially chosen to have a constant Rayleigh cross section.⁶ For this case of constant Rayleigh cross section and varying number density, the Rayleigh signal depends only on the number density, so, from Eq. (1) and relation (5), the local index of refraction varies linearly with the Rayleigh signal:

$$n - 1 \propto S_{\text{Ray}}. \quad (7)$$

In the general combustion case, both N (inversely proportional to temperature) and the effective Rayleigh cross section of the gas mixture, σ_{eff} can vary. For these cases, additional information on the local value of N or σ_{eff} would, in principle, be necessary to determine the value of the local refractive index. As will be seen below, however, a reasonable estimate of the index of refraction field in a turbulent partially premixed hydrocarbon flame can be obtained from the Rayleigh signal alone.

2. Ray-Tracing Algorithm

If a discrete image representing the index of refraction in a flow field is available, it should be possible to simulate the path of the laser beam as it traverses the flow. Snell's law describes the refraction of a ray propagating from a medium with index of refraction n_1 to another medium with n_2 across a planar interface at an angle θ_1 relative to the normal of the interface:

$$n_1 \sin \theta_1 = n_2 \sin \theta_2. \quad (8)$$

Rays are traced across the entire image by using the stencil shown in Fig. 1 to propagate across a pixel (i, j) . The refractive index n_1 is determined by the value of pixel (i, j) . The two-dimensional index gradi-

ent, ∇n , is calculated by using the surrounding pixels for central differencing (Δn_x and Δn_y) and is utilized to obtain the angle β of the interface and the righthand-side index n_2 :

$$\beta = \frac{\pi}{2} - \tan^{-1} \frac{\Delta n_x}{\Delta n_y},$$

$$n_2 = n_1 + \hat{r} \cdot \nabla n, \quad (9)$$

where \hat{r} is the unit vector along the ray before refraction. Snell's law can now be applied to modify the incoming ray's angle and to propagate it to the next pixel, calculating the position with subpixel accuracy. The algorithm allows for the possibility that the ray may cross into row $j + 1$ or $j - 1$. As a ray is traced through the image, a new image is created, with intensity added to a pixel according to the distance the ray travels in crossing the pixel. An alternate approach to the application of Snell's law would be the use of a line of sight integral to obtain the deflection of the ray crossing the medium, as described by Merzkirch.¹³

The correction strategy is then to apply ray tracing across the field of the refractive index to obtain an image representing the redistribution of the incident laser intensity caused by beam steering. Starting on one side (in all examples here, the left-hand side), rays are traced across the entire image. To minimize discretization errors at reasonable computational cost, 10–25 rays per pixel are initialized at the left-hand image boundary, equally spaced in the vertical direction. Including more than this number of rays did not improve the accuracy of the results. Here, a single initial propagation direction is specified, though for a diverging or converging beam it would be important to model the beam's behavior more accurately. In this manner a sheet-intensity distribution is obtained, which is then subjected to smoothing with a Gaussian kernel ($\sigma = 1.14$ pixels) as a zeroth-order approximation to diffraction. In practice, this smoothing also helps to suppress discretization errors. Finally, the original image is corrected by dividing by the result of the ray tracing. There are no free parameters; the only inputs necessary are the index-of-refraction image, the corresponding number of counts in a medium of known refractive index, i.e., an intensity normalization for the image, and the starting angles of the rays. The ray-tracing algorithm was implemented within the open-source image processing software OMA,¹⁴ available at no cost on the World-Wide Web.

There are some assumptions, approximations, and limitations inherent to this approach that will be discussed here before the results for a turbulent flame are described. Since the measurement is two dimensional, any beam deflection in the third dimension is not taken into account. However, for the case to be considered here the flow is (on average) axisymmetric, so the amount of distortion can be estimated if it is assumed that the gradients in the radial and azimuthal directions are equivalent. Similarly, the

finite sheet thickness will lead to broadening of the sheet if the curvature of the iso- n contours is significant within the thickness of the sheet. Again, with the assumption of statistically similar behavior in the radial and azimuthal directions, this effect can be assessed *a posteriori*. In all spatially resolved optical measurements in turbulent flames, there is not only beam steering of the incident laser light but also deflection of the scattered light between the probe volume and the detector. For an axisymmetric flame with known imaging geometry it is possible to quantify the statistical influence of the scattered-ray steering on the image resolution by tracing rays from within the jet back into undisturbed air. Another limitation of the correction scheme presented here is that it uses a simplistic model for diffraction, i.e., altered wave interaction downstream of a refracting gradient. In addition to these concerns on physical grounds, there are problems associated with the discrete nature of the data and measurement noise, which will be discussed below.

Another assumption that has been made in the discussion so far is that the Rayleigh image can be used to infer a realistic index of refraction distribution. To the extent that beam steering introduces stripes into the Rayleigh image that are then interpreted as the true index of refraction distribution, an inaccurate trace can result, which will limit the effectiveness of the final correction. It will be seen below that the types of flow features that are most apt to introduce the stripes in the first place are very similar to the stripes themselves. For this reason, it will turn out that the best performance of the algorithm will be achieved by an iterative application of ray tracing, which will serve to minimize the cumulative effects of the beam steering and improve the final corrected images.

3. Experiment

To test the applicability and accuracy of the ray-tracing approach, a set of Rayleigh imaging data was obtained in a turbulent nonpremixed flame. The flame investigated was a piloted, air-diluted, axisymmetric methane jet flame that has been characterized extensively in an ongoing series of workshops on turbulent nonpremixed flames^{15–18} (specifically, Flame D was measured here). The jet centerline was placed approximately in the center of the imaged region so that each image would contain areas of undisturbed air on both sides of the jet. This centering was also the reason for taking data relatively close to the nozzle 5d downstream from a nozzle with a diameter of 7.2 mm. Characterization of the difference in the noise profiles in quiescent air before and after the illumination sheet traversed the flame allowed us to quantify both the degree of beam steering and the success of the algorithm in correcting it.

Experiments were performed in the Advanced Imaging Laboratory at the Combustion Research Facility at Sandia National Laboratories in Livermore, California. For laser excitation, the combined beams of two frequency-doubled Nd:YAG lasers (1.7 J/pulse total) were formed into a sheet by a 500 mm

focal length cylindrical lens. Rayleigh scattering was imaged onto the chip of an interline transfer camera, gated at 600 ns to suppress flame luminosity. After 2×2 on-chip binning, the resulting useable portion of the images as shown consists of 640×166 pixels with a pixel volume projection of $58 \mu\text{m} \times 58 \mu\text{m} \times 200 \mu\text{m}$. Here, the largest dimension represents an estimate of the average sheet thickness (in quiescent air), which was obtained by inserting a partially reflecting wedge into the beam path to create an image of the sheet cross section on another CCD camera.

Before applying the ray-tracing correction, all standard image corrections were performed. These included (1) subtraction of background and a small average luminosity component that was not gated out by the detector, (2) correction for variations in the average laser-intensity profile as well as nonuniformities in the detector response and optical throughput, and (3) a shot-to-shot laser-intensity profile correction obtained from the portion of the image corresponding to quiescent air before the beam has propagated into the flame (on the left-hand side in the images shown below).

For the air-diluted methane flame considered here, the effective Rayleigh cross section is not constant but varies as the composition changes throughout the flame. Based on tabulated Rayleigh cross sections and species compositions obtained from strained laminar flame calculations, the Rayleigh cross section is expected to vary by $\sim 30\%$ in this flame, with the greatest deviation coming from the unreacted fuel (methane has a cross section 2.2 times larger than air). Since neither the number density nor the effective cross section is fixed, the index of refraction will in general depend on both parameters [see relation (5)]. However, variations in the number density are considerably greater than those for the cross section (the temperature varies by nearly a factor of 7). Consequently, the formulation in relation (7), in which $n - 1$ is taken to be directly proportional to the Rayleigh signal, is expected to yield the best results if a separate measurement of the Rayleigh cross section is not available.

4. Results and Discussion

Figure 2(a) shows one of the images from the data set before any beam-steering corrections have been performed. As the illumination sheet crosses the image, stripes are created by the varying index-of-refraction field. The flow features that contain steep gradients at a shallow angle with respect to the beam propagation direction are particularly likely to mark the start of the sheet nonuniformities that subsequently continue across the image [marked by arrows in Fig. 2(a)].

In order to quantitatively measure the success of the ray-tracing correction, it is useful to define a metric for the success of the technique. In the absence of beam steering, the imaged areas containing quiescent air on the left-hand (L) and right-hand (R) side of the images would have the same noise levels ($N_R = N_L$). Beam steering introduces additional structure on the right-hand side, increasing the noise on that

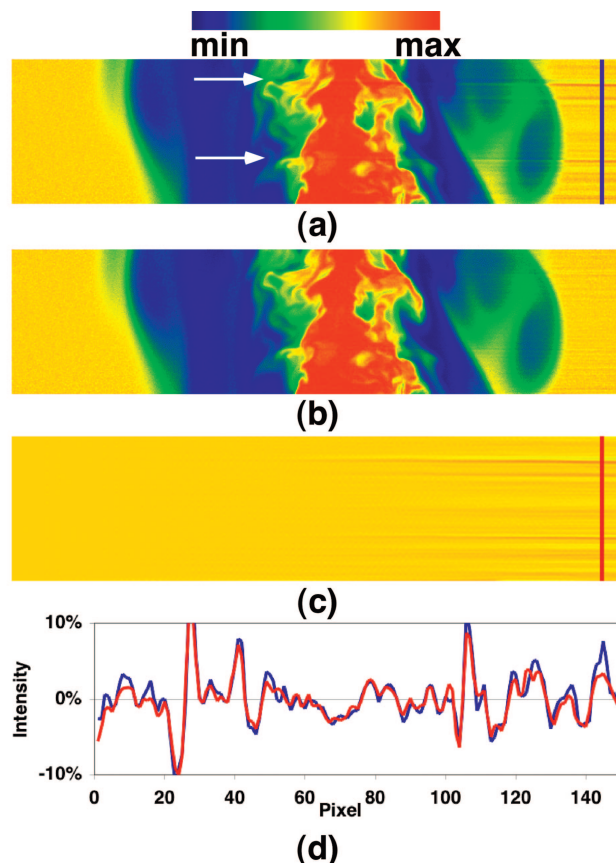


Fig. 2. Single-shot Rayleigh image from a turbulent methane-air jet flame (Flame D) at 5 jet diameters downstream. (a) original image, (b) corrected image using columnwise ray tracing, (c) calculated sheet-intensity deviation based on the columnwise ray-tracing approach, (d) intensity deviation along the vertical line at the right of the images in (a) and (c). Images are $37 \text{ mm} \times 9.6 \text{ mm}$, corresponding to $5.2 \text{ d} \times 1.3 \text{ d}$.

side. A metric for success of the correction is therefore the reduction η_r of this left-to-right degradation, which was normalized here by the left-to-right degradation of the original image according to

$$\eta_r = \frac{(N_R - N_L)_{\text{Orig}} - (N_R - N_L)_{\text{Corr}}}{(N_R - N_L)_{\text{Orig}}} \quad (10)$$

Total reversal of the beam-steering-induced left-to-right image degradation would correspond to $\eta_r = 100\%$, no effect at all to $\eta_r = 0\%$.

Using this metric, the average improvement in the 50-shot image set that was obtained using the ray-tracing algorithm outlined above was $\eta_r = 21\%$. The reason for this relatively modest improvement can be understood by noting the similarity of the image stripes to the flow features that created them. By treating these beam-steering-induced-stripes as part of the actual index-of-refraction distribution, their influence is overestimated—an effect that increases as the distance the beam propagates along the stripes increases.

A more satisfactory result was obtained by modify-

ing the basic ray-tracing algorithm to account for the redistribution of the sheet intensity as the rays were propagated. In the initial implementation, each ray was propagated all the way across the image, and the sheet intensity was determined after 10 to 25 rays per pixel had been traced across the image and their intensities summed. In a modified version, all rays were propagated across a single column of pixels and the resulting intensity distribution in that column was calculated. This distribution was smoothed with a Gaussian kernel ($\sigma = 1.14$ pixels) to remove single-pixel artifacts, propagated one pixel forward, and used to modify the index of refraction distribution that determined subsequent beam-steering effects. This procedure tends to correct for the beam steering as the rays propagate and minimizes the overestimation of the beam steering. Using this columnwise ray-tracing technique, the average value of η_r for the 50-image data set was increased to 78%. Figure 2(b) shows a corrected image obtained using this scheme, and Fig. 2(c) shows the calculated sheet-intensity distribution. Figure 2(d) shows a comparison of the measured and the calculated intensities in air on the right-hand side of the image. The maximum modulation of the sheet intensity in both cases is seen to be just over $\pm 10\%$, with the agreement between the measured and the calculated distribution quite satisfactory.

An iterative approach to removing the stripes caused by the index gradients yielded a further modest improvement in the performance of the ray-tracing technique. In this method, the rays were once again propagated across the image without a forward correction. However, in this implementation the sheet-intensity fluctuations calculated by the ray trace were scaled down to a fraction of their original magnitude in order to eliminate the overcorrection of the stripes caused by beam steering. The scaled-down sheet-intensity image was then used to correct the image. The remaining fluctuations on the right-hand side of the corrected image were then calculated, and if they were lower than in the previous iteration, the process was repeated. When application of the stripe correction caused an increase in the noise on the right-hand side of the image in ambient air, the final correction was discarded, the process was terminated, and the previous iteration taken as the result. Different values of the multiplicative reduction factor were investigated. A value of 0.1 resulted in an optimum sheet correction in 7–9 iterations and resulted in an average $\eta_r = 80\%$ for the 50-image data set. For the data taken here, the improvement in the corrected image probably does not warrant the increased computational time required by the iterative approach. However, it will be shown below that for data with less favorable signal-to-noise ratio (SNR) or poorer spatial resolution the iterative technique may be useful. It should also be noted that the success of the ray-tracing techniques is quite sensitive to the proper angle of propagation of the initial beams. Deviations of 0.1° on either side of the optimum value resulted in a decrease of η_r by $\sim 10\%$.

Most experiments employing Rayleigh imaging do

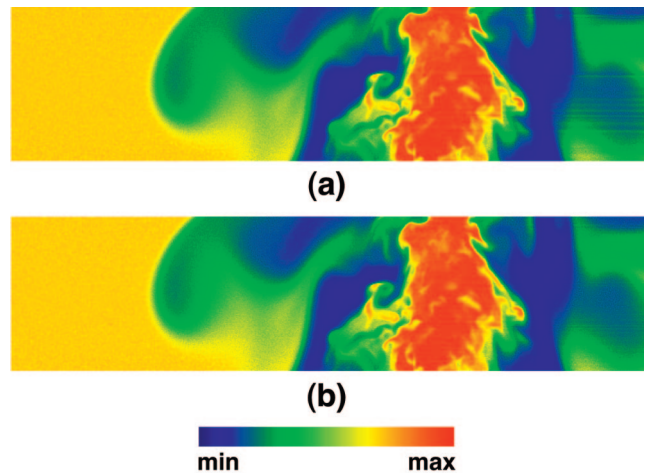


Fig. 3. (a) Rayleigh image from a turbulent flame. (b) Rayleigh image corrected for beam steering by using the iterative ray-tracing algorithm. Images are $37 \text{ mm} \times 9.6 \text{ mm}$.

not record quiescent air on both sides of the image, since doing so tends to reduce the spatial resolution of the measurement and the signal collection efficiency. This was done in this study to provide known reference conditions in order to more easily evaluate the success of the algorithm. It should be noted that neither of the algorithms discussed here require the measurement of constant conditions after the beam passes through the flow to be effective. Application of the columnwise ray-tracing method is the most straightforward—the solution is reached when all columns have been traced. For the iterative algorithm, a test is needed to determine when the optimum correction has been achieved. It was found that the application of a relatively simple high-pass filter operation in a region of the image corresponding to the longest beam path through the flow (on the right-hand side of the image in our case) resulted in an image region representative of the stripes caused by the beam steering. This filtered image region was used to provide a test for stopping the iterations. Figure 3 shows an example of the application of the iterative ray-tracing algorithm to a turbulent flame in which quiescent air was not recorded on both sides of the image.

5. Effects of Noise and Spatial Resolution

It is not always possible to obtain images with such a relatively high SNR as in the Rayleigh images presented here (the single-shot SNR on the left side is 66). Therefore the robustness of the beam-steering correction to noise was investigated by artificially increasing the noise. The uncorrected image was multiplied with a Gaussian-noise image and then corrected by using both the columnwise single-pass and iterative processes described above. Although the noise generated in this way does not yield exactly the scaling of noise to signal that would correspond to increased shot noise, this type of artificial degradation should suffice for the present purposes. For each noise level, the SNRs of the original and the corrected

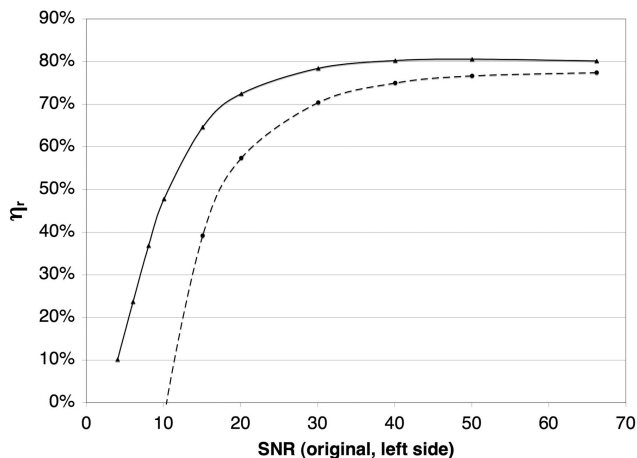


Fig. 4. Performance of the beam-steering correction for different noise levels in the original image. Solid curve, iterative ray-tracing algorithm; dashed curve, columnwise technique. See text for details on the performance measure.

images were evaluated in the undisturbed air on the left- and right-hand side of the images.

Figure 4 shows the behavior of η_r as a function of the SNR for both ray-tracing algorithms. Initially, both correction methods prove to be resistant to increasing the noise in the original image, with the effectiveness η_r remaining roughly constant down to an SNR of about 40. A further increase of the noise affects the performance at first moderately, then more drastically. The performance of the single-pass algorithm falls off more rapidly, with SNR levels of ~ 15 representing the lower limit of effective correction for beam steering. The iterative approach shows some useful improvement down to a SNR of ~ 5 . It is concluded that for high-resolution Rayleigh images a SNR above 10 is sufficient to be able to achieve significant improvement through ray-tracing-based beam-steering correction, particularly using the iterative approach. However, it should be noted that the noise considered here has no pixel-to-pixel spatial correlation. Noise with a larger spatial structure warrants further investigation of the effectiveness of the correction. In particular, photon shot noise originating from the photocathode of an image-intensified detector is often spread over several pixels and could have a more pronounced effect.

In the same way that the SNR of the images in the current data set can be artificially degraded to assess the performance of the correction techniques, the ability of the algorithms to cope with decreased spatial resolution can also be evaluated. From the flame images and sheet-intensity plots of Fig. 2, it is clear that the spatial scale of the stripes approaches the pixel resolution of the image data (the area projected onto each pixel is $58 \mu\text{m} \times 58 \mu\text{m}$; images are 640×166 pixels). By subsampling the images at every 2, 3, or 4 pixels, it is possible to obtain images with increasingly lower spatial resolution while maintaining the same overall SNR. Results are shown in Fig. 5 for both the columnwise and the iterative algorithms. The effec-

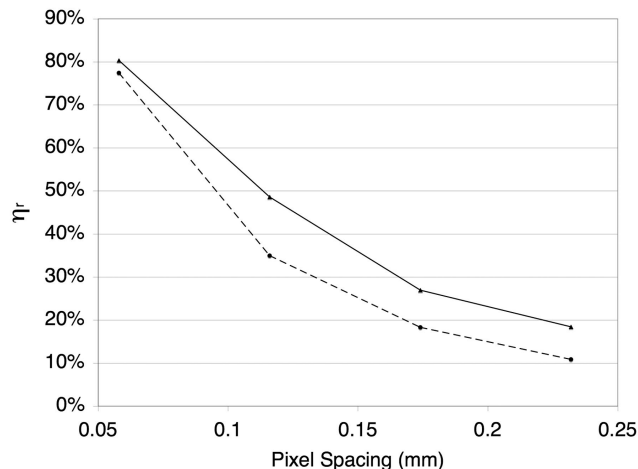


Fig. 5. Performance of the beam-steering correction for different pixel spacings. Solid curve, iterative ray-tracing algorithm; dashed curve, columnwise technique.

tiveness of the correction drops quickly as the spatial resolution of the measurement decreases, emphasizing the importance of resolving the stripes and the gradients of the flow structures to adequately correct for the beam steering. For the flow considered here, the spatial resolution of the original measurement appears to be nearly adequate, though it is not clear how much better the correction would be if higher-resolution data were available. Once again, the iterative algorithm maintains an advantage over the columnwise technique for the range of resolutions investigated. Results obtained by binning the pixels (rather than subsampling) do not change significantly from those shown in Fig. 5, even though there is an increase in the SNR of the binned images. The results summarized in Figs. 4 and 5 suggest that the technique is relatively noise tolerant but suffers considerably from lack of sufficient resolution, a consideration in setting up an experiment utilizing the technique.

6. Simulations

With the validity of the ray-tracing algorithms demonstrated by their ability to adequately predict and correct image stripes, the algorithm and data set can be used to simulate a number of situations relevant to imaging diagnostics. For example, the effect of the index gradients in the flame on the detection of laser light scattered in the probe volume can now be assessed. Figure 6(a) shows the virtual experimental arrangement used. Note that, as in a typical imaging experiment, the orientation of detection and therefore that of the plane displayed in the figure is orthogonal to the laser sheet (the plane the previous figures were in). Rays originating from a point source in the center of the jet are traced through the flame to an ideal collection lens corresponding to an $f/5$ lens imaging at 1:1 magnification onto the plane of detection (this solid angle approximately corresponded to that used in the experiment). The distance of the lens from the probe volume and the lens size could be chosen to be greater, but this would not alter the

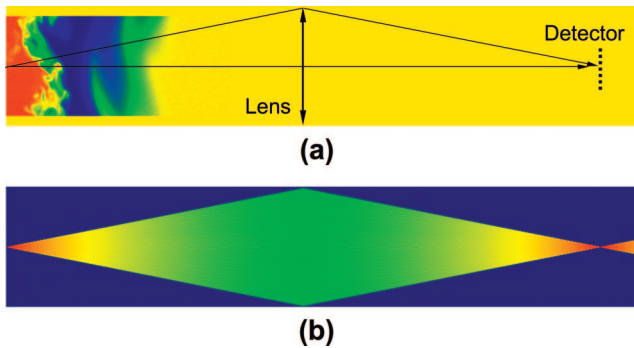


Fig. 6. Ray tracing of scattered light from the probe volume to the detector. (a) Extended Rayleigh image with flame, lens, and detector, (b) corresponding intensity distribution, is displayed in an arbitrary logarithmic color scale corresponding to $\log(\text{rays}/\text{pixel})$. The Spatial coverage of the images is 61 mm \times 12 mm.

results, since once the rays travel in undisturbed air, their angular distribution will remain unchanged. A typical result is shown in Fig. 6(b) as a ray-density image equivalent to Fig. 2(c), but on a logarithmic color scale to account for the large intensity variation in this point-to-point imaging arrangement. At this resolution, there is no effect of the flame on the spread of the focal point, which remains one pixel tall. In fact, the index gradient in the flame has to be increased by more than an order of magnitude to yield spreading beyond one pixel. Thus, for flames of radial dimensions comparable with the ones of this jet flame, beam steering should not be a significant limitation for data collection. However, detection-side beam steering may become non-negligible in high-pressure flames or in geometries with much longer distances between probe volume and flame front.

From Eq. (1) and relation (5) it is seen that $n - 1$ is directly proportional to the number density, N . This suggests that, by scaling the index of refraction calibration constant used in the ray tracing, the images can be used to simulate the beam-steering behavior that would occur at different pressures. This scaling does not take into account changes in spatial scale of the flow that would occur with changes in pressure but does provide some insight into the difficulties that could be expected when going to higher pressure. To investigate pressure effects, the distribution of ray deviations encountered in traversing the turbulent flames was calculated for all of the rays traced in the 50-image data set, first by using the calibration for air and then with a value ten times as large, which would correspond to flames with the same spatial structure at 1 and 10 atm (760 and 7600 Torr). The images used for the simulation were corrected by using the iterative ray-tracing algorithm ($\eta_r = 80\%$), so the effects of stripes should be minimal. The results are shown as a probability density function (pdf) in Fig. 7. The pixel deviation is normalized by the pressure, and it is seen that to within the noise of the pdf, the distributions are the same. The similarity of the pdfs is perhaps not surprising in light of the fact that even at 10 atm, the deflection

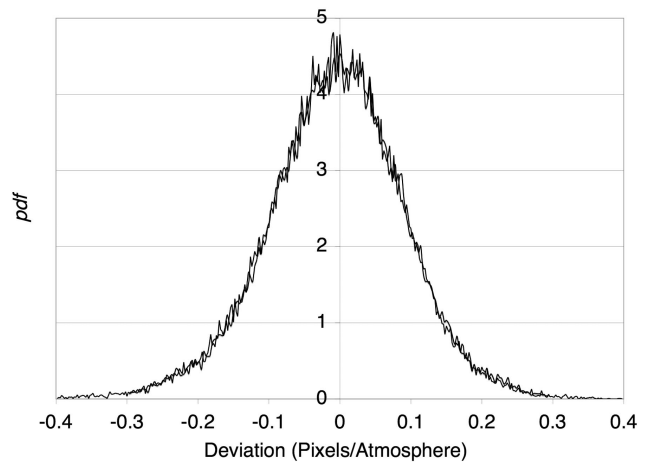


Fig. 7. Deviation of rays propagating across a turbulent flame. Two curves are shown. One for the actual data taken at 1 atm; the second is the simulated behavior at 10 atm. To within the noise of the pdf, the curves are the same.

angles are quite small, as is $n - 1$. For the 1 atm case it is seen that essentially all deviations are less than 0.5 pixel. However, in propagating across the flow field with a pressure of 10 atm, a significant fraction of the rays would undergo deviations of several pixels, which, neglecting diffraction, could lead to gaps in the illumination sheet. The deviations calculated here occur in the plane of the sheet. However, it is expected that similar out-of-plane deviations will occur in these flows as well. If the radial and azimuthal components of the gradient are assumed to be similar, then the pdfs shown could be used to estimate the thickening of the laser sheet caused by out-of-plane gradients.

The ray-tracing algorithm and corrected image data set can also be used to simulate Rayleigh images obtained at high pressure. The atmospheric Rayleigh images [corrected for beam steering as in Fig. 2(b)] are used as a starting point, and the sheet-intensity distribution is calculated by using a calibration factor for $n - 1$ that is ten times that of air (to simulate 10 atm). The calculated sheet-intensity distribution is multiplied by the original image to obtain a predicted, high-pressure Rayleigh image as shown in Fig. 8(a). The same columnwise or iterative ray-tracing algorithms can now be applied to this new image. The result of the application of the columnwise algorithm to the image shown in Fig 8(a) is shown in Fig. 8(b). While the presence of residual stripes in the image is evident, their magnitude has been decreased considerably. At this simulated higher pressure, beam steering causes significantly more structure in the sheet as it traverses the flow, as is made clear from the plot of the sheet-intensity modulation shown in Fig. 8(c). The sheet-intensity fluctuations are now approximately $\pm 80\%$. In the figure, the simulated intensity modulation in air is shown in blue, while the modulation calculated during the ray trace is in red. The average improvement over the 50-shot image set was 59% for the iterative method, while the columnwise technique gave an improvement of $\eta_r = 64\%$.

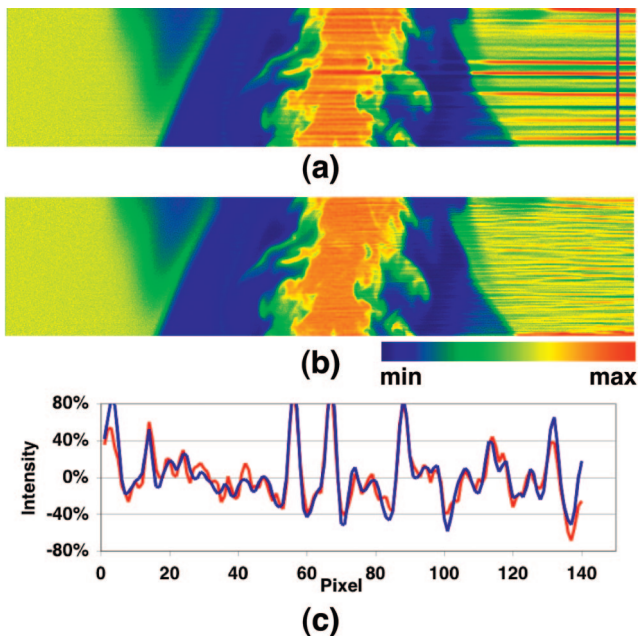


Fig. 8. (a) Simulated Rayleigh image from a 10 atm flame; (b) image corrected by using the columnwise ray-tracing algorithm; (c) blue, sheet-intensity modulation from the right side of the uncorrected image; red, sheet intensity modulation calculated by the ray-tracing algorithm. Images are 37 mm \times 9.6 mm.

7. Conclusions

In turbulent flames, ray tracing is concluded to be a useful tool for correcting beam-steering effects based on Rayleigh images. In general, Rayleigh images allow for an approximate calculation of the index field necessary for ray tracing. For the given image series from a nonpremixed methane-air flame, correction efficiencies of 80% were achieved with an iterative correction scheme. The correction was found to have significant noise tolerance, but a more detailed analysis that would include the effects of spatial scales, both in the flame as well as introduced through the detection process, is desirable. Since the ray-tracing correction is very sensitive to the initial angle, it is important to properly account for the angle of the incoming beam as well as any possible divergence. Rayleigh images of a turbulent flow field can be used with the ray-tracing algorithm to characterize the beam steering between the probe volume and the detector. For the turbulent flame considered here, the effect was found to be negligible. The image data and ray-tracing algorithms presented here were also used to simulate the beam-steering behavior at 10 atm. Since Rayleigh scattering will be generated in any laser imaging experiment, (e.g., PLIF measurements), it may be possible to combine this technique with others to correct for the effects of beam steering on the image.

This research was supported by the Division of Chemical Sciences, Geosciences, and Biosciences, Office of Basic Energy Sciences, U.S. Department of

Energy. The authors thank R. Sigurdsson for assistance during the experiments. Sandia National Laboratories is a multiprogram laboratory operated by Sandia Corporation, a Lockheed Martin Company, for the United States Department of Energy under contract DE-AC04-94-AL85000. The software used and developed in this work is available for free download from the World-Wide Web.¹⁴

References

1. G. Kychakoff, R. Howe, R. K. Hanson, and J. McDaniel, "Quantitative visualization of combustion species in a plane," *Appl. Opt.* **21**, 3225–3227 (1982).
2. G. Kychakoff, R. Howe, R. K. Hanson, M. Drake, R. Pitz, M. Lapp, and C. Penney, "Visualization of turbulent flame fronts with planar laser-induced fluorescence," *Science* **224**, 382–384 (1984).
3. R. K. Hanson, "Combustion diagnostics: planar imaging techniques," *Proc. Combust. Inst.* **21**, 1677–1691 (1986).
4. M. C. Escoda and M. B. Long, "Rayleigh scattering measurements of the gas concentration field in turbulent jets," *AIAA J.* **21**, 81–84 (1983).
5. D. R. Dowling and P. E. Dimotakis, "Similarity of the concentration field of gas-phase turbulent jets," *J. Fluid Mech.* **218**, 109–141 (1990).
6. R. W. Dibble and R. E. Hollenbach, "Laser Rayleigh thermometry in turbulent flames," *Proc. Combust. Inst.* **18**, 1489–1499 (1981).
7. D. C. Fourchette, R. M. Zurn, and M. B. Long, "Two-dimensional Rayleigh thermometry in a turbulent nonpremixed methane hydrogen flame," *Combust. Sci. Tech.* **44**, 307–317 (1986).
8. V. Bergmann, W. Meier, D. Wolff, and W. Stricker, "Application of spontaneous Raman and Rayleigh scattering and 2D LIF for the characterization of a turbulent $\text{CH}_4/\text{H}_2/\text{N}_2$ jet diffusion flame," *Appl. Phys. B* **66**, 489–502 (1998).
9. Y.-C. Chen and M. S. Mansour, "Topology of turbulent premixed flame fronts resolved by simultaneous planar imaging of LIPF of OH radical and Rayleigh scattering," *Exp. Fluids* **26**, 277–287 (1999).
10. J. Fielding, J. H. Frank, S. A. Kaiser, and M. B. Long, "Polarized/depolarized Rayleigh scattering for determining fuel concentrations in flames," *Proc. Combust. Inst.* **29**, 2703–2709 (2002).
11. R. B. Miles, W. R. Lempert, and J. N. Forkey, "Laser Rayleigh scattering," *Meas. Sci. Technol.* **12**, R33–R51 (2001).
12. P. E. Dimotakis, H. J. Catrakis, and D. C. Fourchette, "Flow structure and optical beam propagation in high-Reynolds-number gas-phase shear layers and jets," *J. Fluid Mech.* **433**, 105–134 (2001).
13. W. Merzkirch, *Flow visualization* (Academic, 1974).
14. P. A. Kalt and M. B. Long, "OMA—image processing for Mac OS X," www.oma-x.org (accessed May 2005; includes the ray-tracing algorithms used here).
15. R. S. Barlow, ed., "International workshop on measurement and computation of turbulent nonpremixed flames," www.ca.sandia.gov/TNF/ (accessed May 2005).
16. R. S. Barlow and J. H. Frank, "Effects of turbulence on species mass fractions in methane/air jet flames," *Proc. Combust. Inst.* **27**, 1087–1095 (1998).
17. A. N. Karpetis and R. S. Barlow, "Measurements of scalar dissipation in a turbulent piloted methane/air jet flame," *Proc. Combust. Inst.* **29**, 1929–1936 (2002).
18. J. H. Frank, S. A. Kaiser, and M. B. Long, "Reaction-rate, mixture-fraction, and temperature imaging in turbulent methane/air jet flames," *Proc. Combust. Inst.* **29**, 2687–2694 (2002).